Journal of Computational Physics 291 (2015) 82–98

Contents lists available at ScienceDirect

Journal of Computational Physics

www.elsevier.com/locate/jcp

Fully discrete energy stable high order finite difference methods for hyperbolic problems in deforming domains

Samira Nikkar *, Jan Nordström

Department of Mathematics, Computational Mathematics, Linköping University, SE-581 83 Linköping, Sweden

ARTICLE INFO

Article history:
Received 15 October 2014
Received in revised form 26 January 2015
Accepted 18 February 2015
Available online 26 February 2015

Keywords:
Deforming domain
Initial boundary value problems
High order accuracy
Well-posed boundary conditions
Summation-by-parts operators
Stability
Convergence
Conservation
Numerical geometric conservation law
Euler equation
Sound propagation

ABSTRACT

A time-dependent coordinate transformation of a constant coefficient hyperbolic system of equations which results in a variable coefficient system of equations is considered. By applying the energy method, well-posed boundary conditions for the continuous problem are derived. Summation-by-Parts (SBP) operators for the space and time discretization, together with a weak imposition of boundary and initial conditions using Simultaneously Approximation Terms (SATs) lead to a provable fully-discrete energy-stable conservative finite difference scheme.

We show how to construct a time-dependent SAT formulation that automatically imposes boundary conditions, when and where they are required. We also prove that a uniform flow field is preserved, i.e. the Numerical Geometric Conservation Law (NGCL) holds automatically by using SBP-SAT in time and space. The developed technique is illustrated by considering an application using the linearized Euler equations: the sound generated by moving boundaries. Numerical calculations corroborate the stability and accuracy of the new fully discrete approximations.

1. Introduction

High order SBP operators together with weak implementation of boundary conditions by SATs, can efficiently and reliably handle large problems on structured grids for reasonably smooth geometries [1–7]. The main reason to use weak boundary procedures together with SBP operators and the energy method is the fact that with this combination, provable stable schemes can be constructed. For comprehensive reviews of the SBP-SAT schemes, see [8,9].

The developments described above have so far dealt mostly with steady problems while computing flow-fields around moving and deforming objects involves time-dependent meshes [10–12]. We have previously treated the problems with steady coordinate transformations [11,5,6]. In this paper we take the next step, which is the treatment of time-dependent transformations in combination with SBP-SAT schemes. To guarantee stability of the fully discrete approximation we employ the recently developed SBP-SAT technique in time [13,14].

The hyperbolic constant coefficient system that we consider, represents wave propagation problems governed by for example the elastic wave equation [15,6], Maxwell's equations [16,17,4] and the linearized Euler equations [18–20].

The rest of this paper proceeds as follows. In Section 2, we analyze the continuous problem which undergoes a transformation from a deforming domain into a fixed domain, and derive characteristic boundary conditions which lead to a strongly

* Corresponding author.
E-mail addresses: samira.nikkar@liu.se (S. Nikkar), jan.nordstrom@liu.se (J. Nordström).

http://dx.doi.org/10.1016/j.jcp.2015.02.027
0021-9991/

well-posed problem. Section 3 deals with the discrete problem where we guarantee stability, conservation and the validity of the NGCL. In Section 4, numerical examples which corroborate the previous theoretical development and confirm the accuracy and stability of the scheme are considered. An application where sound is generated and propagated by a moving boundary is also studied. Finally we draw conclusions in Section 5.

2. The continuous problem

Consider the following constant coefficient system,

$$V_t + (\hat{A}V)_x + (\hat{B}V)_y = 0, \quad (x, y) \in \Phi(t), \quad t \in [0, T], \tag{1}$$

where the spatial domain Φ is time-dependent. We assume for simplicity that the constant matrices $\hat{A}$ and $\hat{B}$ are symmetric and of size l. If the original problem is not symmetric, we symmetrize it by the procedure in [18].

A time-dependent transformation from the Cartesian coordinates into curvilinear coordinates, which results in a fixed spatial domain, is

$$\begin{aligned} &x = x(\tau, \xi, \eta), \quad y = y(\tau, \xi, \eta), \quad t = \tau, \\ &\xi = \xi(t, x, y), \quad \eta = \eta(t, x, y), \quad \tau = t. \end{aligned} \tag{2}$$

The chain-rule is employed to interpret the system (1) in terms of the curvilinear coordinates as

$$V_\tau + (\xi_t I + \xi_x \hat{A} + \xi_y \hat{B})V_\xi + (\eta_t I + \eta_x \hat{A} + \eta_y \hat{B})V_\eta = 0, \tag{3}$$

where $0 \le \xi \le 1,\ 0 \le \eta \le 1,\ 0 \le \tau \le T$. The Jacobian matrix of the transformation is

$$[J] = \begin{pmatrix} x_\xi & y_\xi & 0 \\ x_\eta & y_\eta & 0 \\ x_\tau & y_\tau & 1 \end{pmatrix}, \tag{4}$$

where $(V_\xi, V_\eta, V_\tau)^T = [J](V_x, V_y, V_t)^T$. The relation between $[J]$, and its inverse, which transforms the derivatives back to the Cartesian coordinates leads to the metric relations

$$\begin{aligned} &J\xi_t = x_\eta y_\tau - x_\tau y_\eta, \quad J\xi_x = y_\eta, \quad J\xi_y = -x_\eta \\ &J\eta_t = y_\xi x_\tau - x_\xi y_\tau, \quad J\eta_x = -y_\xi, \quad J\eta_y = x_\xi, \end{aligned} \tag{5}$$

in which $J = x_\xi y_\eta - x_\eta y_\xi > 0$ is the determinant of $[J]$.

By multiplying (3) with J and using (5), we replace the coefficients in terms of derivatives of the curvilinear coordinates. Eq. (3) can be rewritten as

$$\begin{aligned} &(JV)_\tau + [(J\xi_t I + J\xi_x \hat{A} + J\xi_y \hat{B})V]_\xi + [(J\eta_t I + J\eta_x \hat{A} + J\eta_y \hat{B})V]_\eta \\ &\quad = [J_\tau + (J\xi_t)_\xi + (J\eta_t)_\eta]V + [(J\xi_x)_\xi + (J\eta_x)_\eta]\hat{A}V + [(J\xi_y)_\xi + (J\eta_y)_\eta]\hat{B}V, \end{aligned} \tag{6}$$

where I denotes the identity matrix of size l. All non-singular coordinate transformations fulfill the Geometric Conservation Law (GCL) [10,21,22], which is summarized as

$$\begin{aligned} &J_\tau + (J\xi_t)_\xi + (J\eta_t)_\eta = 0, \\ &(J\xi_x)_\xi + (J\eta_x)_\eta = 0, \\ &(J\xi_y)_\xi + (J\eta_y)_\eta = 0. \end{aligned} \tag{7}$$

The right hand side of (6) is identically zero, due to (7), which results in the conservative form of the system.

The final problem in the presence of initial and boundary conditions that we will consider in this paper is

$$\begin{aligned} (JV)_\tau + (AV)_\xi + (BV)_\eta &= 0, && (\xi, \eta) \in \Omega, && \tau \in [0, T], \\ LV &= g(\tau, \xi, \eta), && (\xi, \eta) \in \delta\Omega, && \tau \in [0, T], \\ V &= f(\xi, \eta), && (\xi, \eta) \in \Omega, && \tau = 0, \end{aligned} \tag{8}$$

where

$$A = J\xi_t I + J\xi_x \hat{A} + J\xi_y \hat{B}, \quad B = J\eta_t I + J\eta_x \hat{A} + J\eta_y \hat{B}, \tag{9}$$

and $\Omega = [0, 1] \times [0, 1]$. In (8), L is the boundary operator, g is the boundary data and f is the initial data.

2.1. Well-posedness

The energy method (multiply with the transpose of the solution and integrate over the domain Ω and time-interval $[0,\ T]$) applied to (8) leads to

$$\int_0^T \iint_\Omega [V^T(JV)_\tau + V^T(AV)_\xi + V^T(BV)_\eta]\, d\xi\, d\eta\, d\tau = 0. \tag{10}$$

By adding and subtracting $V_\tau^T JV + V_\xi^T AV + V_\eta^T BV$ to the integral argument in (10), we get

$$\int_0^T \iint_\Omega [(V^T JV)_\tau + (V^T AV)_\xi + (V^T BV)_\eta]\, d\xi\, d\eta\, d\tau = \int_0^T \iint_\Omega [(V_\tau^T JV) + (V_\xi^T AV) + (V_\eta^T BV)]\, d\xi\, d\eta\, d\tau. \tag{11}$$

However, the right hand side of (11) is zero, since the matrices J, A and B are symmetric, and V solves equation $JV_\tau + AV_\xi + BV_\eta = 0$. The latter can be seen by multiplying (3) with J and using (9). Integration of (11), and the use of Green–Gauss theorem, yields

$$||V(T,\xi,\eta)||_J^2 = ||f(\xi,\eta)||_J^2 - \int_0^T \oint_{\delta\Omega} V^T[(A,B)\cdot n]\, V\ ds\, d\tau, \tag{12}$$

where the norm is defined by $||V||_J^2 = \iint_\Omega V^T J\ V\, d\xi\, d\eta$. In (12), $n = (n_1,\ n_2)$ is the unit normal vector pointing outward from Ω, $(A,\ B)\cdot n = n_1 A + n_2 B$ and ds is an infinitesimal element along the boundary of Ω.

In order to bound the energy of the solution, boundary conditions must be applied when the matrix $C = (A,B)\cdot n$ is negative definite. We decompose $C = X\Lambda_C X^T = X\Lambda_C^+ X^T + X\Lambda_C^- X^T = C^+ + C^-$ where Λ_C^+ and Λ_C^- are diagonal matrices with positive and negative eigenvalues of C, respectively, on the main diagonal. The energy of the solution is now bounded by data if we impose the characteristic boundary conditions

$$(X^T V)_i = (X^T V_\infty)_i, \quad (\Lambda_C)_{ii} < 0, \tag{13}$$

where the vector V_∞ is the solution at the boundary $\delta\Omega$. The continuous energy, using (13) becomes

$$||V(T,\xi,\eta)||_J^2 = ||f(\xi,\eta)||_J^2 - \int_0^T \oint_{\delta\Omega} V_\infty^T C^- V_\infty\, ds\, d\tau - \int_0^T \oint_{\delta\Omega} V^T C^+ V\, ds\, d\tau. \tag{14}$$

The estimate (14) guarantees uniqueness of the solution and existence is given by the fact that we use the correct number of boundary conditions. Hence we can summarize the results obtained so far in the following proposition.

Proposition 1. *The continuous problem (8) with the boundary condition in (13) is strongly well-posed and has the bound (14).*

Remark 1. The problem (6) is called strongly well-posed since we have an estimate of the solution also for non-zero boundary data. For more details on well-posedness see [23].

As an example, assume that we only need boundary conditions at the south boundary, see Fig. 1, indicated by subscript s, then $C_s = (A,B)_s\cdot(0,-1) = -B_s = -X_s\Lambda_{B_s}X_s^T$, and (14) becomes

$$||V(T,\xi,\eta)||_J^2 = ||f(\xi,\eta)||_J^2 + \int_0^T \int_0^1 V_\infty^T B_s^+ V_\infty\, d\xi\, d\tau + \int_0^T \int_0^1 V_s^T B_s^- V_s\, d\xi\, d\tau. \tag{15}$$

3. The discrete problem

The spatial computational domain Ω is a square in ξ, η coordinates, see Fig. 1, and discretized using N and M nodes in the direction of ξ and η respectively. In time we use L time levels from 0 to T. The fully-discrete numerical solution is a column vector of size $lLMN$ organized as follows

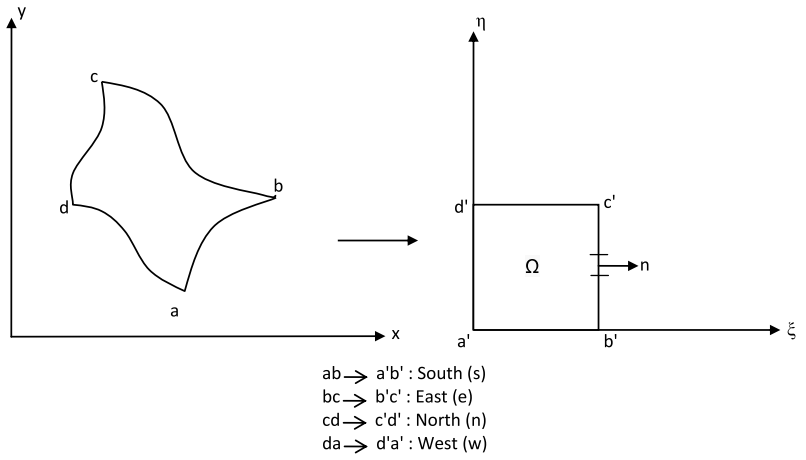

Fig. 1. A schematic of the moving and fixed domains and boundary definitions.

$$\mathbf{V} = \begin{bmatrix} V_0 \\ \vdots \\ [V_k] \\ \vdots \\ V_L \end{bmatrix}; \quad [V_k] = \begin{bmatrix} V_0 \\ \vdots \\ [V_i] \\ \vdots \\ V_N \end{bmatrix}_k; \quad [V_i]_k = \begin{bmatrix} V_0 \\ \vdots \\ [V_j] \\ \vdots \\ V_M \end{bmatrix}_{ki}; \quad [V_j]_{ki} = \begin{bmatrix} v_1 \\ v_2 \\ \vdots \\ v_l \end{bmatrix}_{kij} = V_{kij}, \tag{16}$$

where $V_{kij} = [v_1, v_2, \cdots, v_l]^T_{kij}$ approximates $V(\tau_k, \xi_i, \eta_j)$.

The first derivative u_ξ is approximated by $D_\xi \mathbf{u}$, where D_ξ is a so-called SBP operator of the form

$$D_\xi = P_\xi^{-1} Q_\xi, \tag{17}$$

and $\mathbf{u} = [u_0, u_1, \cdots, u_N]^T$ is the solution evaluated in each grid point. P_ξ is a symmetric positive definite matrix, and Q is an almost skew-symmetric matrix that satisfies

$$Q_\xi + Q_\xi^T = E_1 - E_0 = B = diag(-1, 0, ..., 0, 1). \tag{18}$$

In (18), $E_0 = diag(1, 0, \ldots, 0)$ and $E_1 = diag(0, \ldots, 0, 1)$. The η and τ directions are discretized in the same way.

A first derivative SBP operator is a $2s$-order accurate central difference operator which is modified close to the boundaries such that it becomes one-sided. Together with a diagonal norm P, the boundary closure is s-order accurate, making a stable first order approximation $s+1$ order accurate globally [24,25]. For more non-standard SBP operators see [26–29].

A finite difference approximation including the time discretization [13], on SBP-SAT form, is constructed by extending the one-dimensional SBP operators in a tensor product fashion as

$$\begin{aligned} D_\tau &= P_\tau^{-1} Q_\tau \otimes I_\xi \otimes I_\eta \otimes I, \\ D_\xi &= I_\tau \otimes P_\xi^{-1} Q_\xi \otimes I_\eta \otimes I, \\ D_\eta &= I_\tau \otimes I_\xi \otimes P_\eta^{-1} Q_\eta \otimes I \end{aligned} \tag{19}$$

where $\otimes$ represents the Kronecker product [30]. All matrices in the first position are of size $L \times L$, the second position $N \times N$, the third position $M \times M$ and the fourth position $l \times l$. I denotes the identity matrix with a size consistent with its position in the Kronecker product.

The Kronecker product is bilinear and associative. For square matrices the following rules exist

$$(A \otimes B)(C \otimes D) = (AC \otimes BD), \quad (A \otimes B)^{-1} = A^{-1} \otimes B^{-1}, \quad (A \otimes B)^T = A^T \otimes B^T. \tag{20}$$

For later reference we need

Lemma 1. *The difference operators in (19) commute.*

Proof. The properties (20) of the Kronecker product lead to

$$\begin{aligned} D_\tau D_\xi &= (P_\tau^{-1} Q_\tau \otimes I_\xi \otimes I_\eta \otimes I)(I_\tau \otimes P_\xi^{-1} Q_\xi \otimes I_\eta \otimes I) \\ &= P_\tau^{-1} Q_\tau \otimes P_\xi^{-1} Q_\xi \otimes I_\eta \otimes I \\ &= (I_\tau \otimes P_\xi^{-1} Q_\xi \otimes I_\eta \otimes I)(P_\tau^{-1} Q_\tau \otimes I_\xi \otimes I_\eta \otimes I) = D_\xi D_\tau. \end{aligned}$$

The proof is analogous for the other coordinate combinations. □

To obtain an energy estimate similar to the continuous one, we use the splitting technique described in [31]. We split the equation in (8) as

$$\tfrac{1}{2}[(JV)_\tau + JV_\tau + J_\tau V] + \tfrac{1}{2}[(AV)_\xi + AV_\xi + A_\xi V] + \tfrac{1}{2}[(BV)_\eta + BV_\eta + B_\eta V] = 0. \tag{21}$$

The SBP-SAT approximation of (21) including the penalty terms for the boundary procedure (we only consider the south boundary), and a weak initial condition, is constructed as

$$\begin{aligned} &\tfrac{1}{2}[D_\tau(\mathbf{JV}) + \mathbf{J}D_\tau\mathbf{V} + \mathbf{J}_\tau\mathbf{V}] + \tfrac{1}{2}[D_\xi(\mathbf{AV}) + \mathbf{A}D_\xi\mathbf{V} + \mathbf{A}_\xi\mathbf{V}] + \tfrac{1}{2}\,[D_\eta(\mathbf{BV}) + \mathbf{B}D_\eta\mathbf{V} + \mathbf{B}_\eta\mathbf{V}] \\ &\quad = \tilde{P}_i^{-1}\Sigma_i(\mathbf{V} - \mathbf{f}) + \tilde{P}_s^{-1}\Sigma_s\mathbf{X}_s^T[\mathbf{V} - \mathbf{V}_\infty]. \end{aligned} \tag{22}$$

In (22), $\mathbf{J}$ and $\mathbf{J}_\tau$ are diagonal matrices approximating J and J_τ values pointwise. Moreover, $\mathbf{A}$, $\mathbf{B}$, $\mathbf{A}_\xi$ and $\mathbf{B}_\eta$ are block-diagonal matrices approximating A, B, A_ξ and B_η pointwise respectively, i.e.

$$\begin{aligned} \mathbf{A}_\xi &= \begin{bmatrix} (\mathbf{A}_\xi)_0 & & & \\ & \ddots & & \\ & & (\mathbf{A}_\xi)_k & \\ & & & \ddots \\ & & & & (\mathbf{A}_\xi)_L \end{bmatrix}; \\ (\mathbf{A}_\xi)_k &= \begin{bmatrix} (\mathbf{A}_\xi)_0 & & & \\ & \ddots & & \\ & & (\mathbf{A}_\xi)_i & \\ & & & \ddots \\ & & & & (\mathbf{A}_\xi)_N \end{bmatrix}_k; \\ (\mathbf{A}_\xi)_{ik} &= \begin{bmatrix} (\mathbf{A}_\xi)_0 & & & \\ & \ddots & & \\ & & (\mathbf{A}_\xi)_j & \\ & & & \ddots \\ & & & & (\mathbf{A}_\xi)_M \end{bmatrix}_{ki}; \end{aligned} \tag{23}$$

$$(\mathbf{A}_\xi)_{kij} \approx A_\xi(\tau_k, \xi_i, \eta_j). \tag{24}$$

Note that in (24),

$$\begin{aligned} (\mathbf{A}_\xi)_{kij} &= [\overline{(J\xi_t)_\xi} + \overline{(J\xi_x)_\xi}\hat{A} + \overline{(J\xi_y)_\xi}\hat{B}]_{kij} \\ (\mathbf{B}_\eta)_{kij} &= [\overline{(J\eta_t)_\eta} + \overline{(J\eta_x)_\eta}\hat{A} + \overline{(J\eta_y)_\eta}\hat{B}]_{kij}, \end{aligned} \tag{25}$$

where $\overline{(J\xi_t)_\xi}$, $\overline{(J\xi_x)_\xi}$, $\overline{(J\xi_y)_\xi}$, $\overline{(J\eta_t)_\eta}$, $\overline{(J\eta_x)_\eta}$ and $\overline{(J\eta_y)_\eta}$ approximate $(J\xi_t)_\xi$, $(J\xi_x)_\xi$, $(J\xi_y)_\xi$, $(J\eta_t)_\eta$, $(J\eta_x)_\eta$ and $(J\eta_y)_\eta$ pointwise respectively. In (22), the variables with a bold face correspond to the ones with regular face in the continuous problem. This notation is employed to be able to use similar names for the variables that are inherently (not exactly) the same in the continuous and the discrete problem, regardless of the structure of the variables.

Moreover, Σ_i and Σ_s are the penalty matrices corresponding to the weak initial condition and the south boundary procedure. Furthermore $\tilde{P}_i^{-1} = P_\tau^{-1}E_0 \otimes I_\xi \otimes I_\eta \otimes I$, $\tilde{P}_s^{-1} = I_\tau \otimes I_\xi \otimes P_\eta^{-1}E_0 \otimes I$, and $\mathbf{X}_s = (I_\tau \otimes I_\xi \otimes E_0 \otimes X)$. All the numerical matrices defined so far are of size $lLMN \times lLMN$. $\mathbf{V}_\infty$ is a zero vector of the same size as V except at the position $\eta = 0$ where the zeros are replaced with the boundary data. Moreover $\mathbf{f}$ is a zero vector, of the same size as V, except at the position $\tau = 0$ where the initial data (compatible with the reference solution at the boundaries) is imposed.

3.1. Stability

The energy method (multiplying from the left with $\mathbf{V}^T(P_\tau \otimes P_\xi \otimes P_\eta \otimes I)$) is applied to (22), the properties (20) are employed and the equation is added to its transpose. The result is

$$\begin{aligned}
&\mathbf{V}^T(\tilde{B}_\tau \mathbf{J} + \tilde{B}_\xi \mathbf{A} + \tilde{B}_\eta \mathbf{B})\mathbf{V} + \mathbf{V}^T\tilde{P}(\mathbf{J}_\tau + \mathbf{A}_\xi + \mathbf{B}_\eta)\mathbf{V} \\
&= \mathbf{V}^T(E_0 \otimes P_\xi \otimes P_\eta \otimes I)\Sigma_i(\mathbf{V} - \mathbf{f}) + (\mathbf{V} - \mathbf{f})^T\Sigma_i^T(E_0 \otimes P_\xi \otimes P_\eta \otimes I)\mathbf{V} \\
&\quad + \mathbf{V}^T(P_\tau \otimes P_\xi \otimes E_0 \otimes I)\Sigma_s\mathbf{X}_s^T[\mathbf{V} - \mathbf{V}_\infty] + [\mathbf{V} - \mathbf{V}_\infty]^T\mathbf{X}_s\Sigma_s^T(P_\tau \otimes P_\xi \otimes E_0 \otimes I)\mathbf{V},
\end{aligned} \tag{26}$$

where $\tilde{P} = (P_\tau \otimes P_\xi \otimes P_\eta \otimes I)$, $\tilde{B}_\tau = [(Q + Q^T)_\tau \otimes P_\xi \otimes P_\eta \otimes I]$, $\tilde{B}_\xi = [P_\tau \otimes (Q + Q^T)_\xi \otimes P_\eta \otimes I]$, and $\tilde{B}_\eta = [P_\tau \otimes P_\xi \otimes (Q + Q^T)_\eta \otimes I]$. We have used that the diagonal matrices $\tilde{B}_\tau$, $\tilde{B}_\xi$ and $\tilde{B}_\eta$ commute with the symmetric matrices **J**, **A** and **B** respectively.

We will need

Lemma 2. *The NGCL:* $\mathbf{J}_\tau + \mathbf{A}_\xi + \mathbf{B}_\eta = 0$, *holds.*

Proof. Consider the following definitions,

$$\begin{aligned}
\mathbf{J}_\tau &= diag[D_\tau(D_\eta M^{(1)} - D_\xi M^{(2)})] \\
\overline{(J\xi_t)_\xi} &= diag[D_\xi(D_\tau M^{(2)} - D_\eta M^{(3)})] \\
\overline{(J\eta_t)_\eta} &= diag[D_\eta(D_\xi M^{(3)} - D_\tau M^{(1)})] \\
\overline{(J\xi_x)_\xi} &= diag[D_\xi(D_\eta \mathbf{y})] \\
\overline{(J\xi_y)_\xi} &= diag[-D_\xi(D_\eta \mathbf{x})] \\
\overline{(J\eta_x)_\eta} &= diag[-D_\eta(D_\xi \mathbf{y})] \\
\overline{(J\eta_y)_\eta} &= diag[D_\eta(D_\xi \mathbf{x})]
\end{aligned} \tag{27}$$

in which **x** and **y** are the discrete Cartesian coordinates in Φ. Also $M^{(1)} = diag(\mathbf{y})(D_\xi \mathbf{x})$, $M^{(2)} = diag(\mathbf{y})(D_\eta \mathbf{x})$ and $M^{(3)} = diag(\mathbf{y})(D_\tau \mathbf{x})$. We evaluate the term $\mathbf{J}_\tau + \mathbf{A}_\xi + \mathbf{B}_\eta$, and substitute $\mathbf{A}_\xi$ and $\mathbf{B}_\eta$ with the definitions (24) and (25), which results in

$$\mathbf{J}_\tau + \mathbf{A}_\xi + \mathbf{B}_\eta = \mathbf{J}_\tau + \overline{(J\xi_t)_\xi} + \left[\overline{(J\xi_x)_\xi} + \overline{(J\eta_x)_\eta}\right]\hat{\mathbf{A}} + \overline{(J\eta_t)_\eta} + \left[\overline{(J\xi_y)_\xi} + \overline{(J\eta_y)_\eta}\right]\hat{\mathbf{B}}, \tag{28}$$

where $\hat{\mathbf{A}} = I_\tau \otimes I_\xi \otimes I_\eta \otimes \hat{A}$, $\hat{\mathbf{B}} = I_\tau \otimes I_\xi \otimes I_\eta \otimes \hat{B}$. Now we insert (27) into (28) and obtain

$$\begin{aligned}
\mathbf{J}_\tau + \mathbf{A}_\xi + \mathbf{B}_\eta &= diag[D_\tau(D_\eta M^{(1)} - D_\xi M^{(2)})] + diag[D_\xi(D_\tau M^{(2)} - D_\eta M^{(3)})] \\
&\quad + diag[D_\xi(D_\eta \mathbf{y}) - D_\eta(D_\xi \mathbf{y})]\hat{\mathbf{A}} + diag[D_\eta(D_\xi M^{(3)} - D_\tau M^{(1)})] \\
&\quad + diag[D_\eta(D_\xi \mathbf{x}) - D_\xi(D_\eta \mathbf{x})]\hat{\mathbf{B}}.
\end{aligned} \tag{29}$$

By Lemma 1 we find that the right hand side of (29) is zero. □

Remark 2. The NGCL as a consequence of commuting operators is previously reported in [32].

On the left hand side of the equality in (26), we keep the terms corresponding to the initial time, final time and the south boundary and ignore the other boundary terms. By also using Lemma 2 we get

$$\begin{aligned}
\mathbf{V}^T\mathbf{J}(E_L \otimes P_\xi \otimes P_\eta \otimes I)\mathbf{V} &= \mathbf{V}^T(E_0 \otimes P_\xi \otimes P_\eta \otimes I)(\mathbf{J} + 2\Sigma_i)\mathbf{V} - \mathbf{f}^T(E_0 \otimes P_\xi \otimes P_\eta \otimes I)\Sigma_i\mathbf{V} \\
&\quad - \mathbf{V}^T(E_0 \otimes P_\xi \otimes P_\eta \otimes I)\Sigma_i\mathbf{f} + \mathbf{V}^T(P_\tau \otimes P_\xi \otimes E_0 \otimes I)(\mathbf{B_s} + \Sigma_s\mathbf{X}_s^T + \mathbf{X}_s\Sigma_s^T)V \\
&\quad - \mathbf{V}^T(P_\tau \otimes P_\xi \otimes E_0 \otimes I)\Sigma_s\mathbf{X}_s^T(\mathbf{V}_\infty)_s - (\mathbf{V}_\infty)_s^T\mathbf{X}_s\Sigma_s^T(P_\tau \otimes P_\xi \otimes E_0 \otimes I)\mathbf{V}.
\end{aligned} \tag{30}$$

In (30), $\mathbf{B}_s = (I_\tau \otimes I_\xi \otimes E_0 \otimes I)\mathbf{B}$, and E_0, E_L are zero matrices except at the one entry corresponding to the initial and final time, respectively.

We can prove

Proposition 2. *The discrete problem (22) is stable if*

$$\mathbf{J} + 2\Sigma_i \le 0, \;\; \Sigma_s\mathbf{X}_s^T + \mathbf{X}_s\Sigma_s^T + \mathbf{B}_s \le 0 \tag{31}$$

holds.

Proof. With zero boundary and initial data the solution at the final time is clearly bounded. □

A particularly nice result is obtained with $\Sigma_i = -\mathbf{J}$. Let $\Sigma_s = \mathbf{X}_s \tilde{\Sigma}_s$, where $\mathbf{X}_s = (I_\tau \otimes I_\xi \otimes E_0 \otimes I)\mathbf{X}$, $\mathbf{X}$ is a block diagonal matrix of X and $\tilde{\Sigma}_s$ is diagonal. By inserting $\mathbf{B}_s = \mathbf{X}_s \Lambda_\mathbf{B} \mathbf{X}_s^T$, the second condition in (31) becomes $\mathbf{X}_s(2\tilde{\Sigma}_s + \Lambda_{\mathbf{B}_s})\mathbf{X}_s^T \leq 0$, and is fulfilled if $\tilde{\Sigma}_s$ is defined such that the following relations hold,

$$\begin{aligned} (\tilde{\Sigma}_s)_{ii} &\leq -\frac{(\Lambda_{\mathbf{B}_s})_{ii}}{2} \quad \text{if} \quad (\Lambda_{\mathbf{B}_s})_{ii} > 0 \\ (\tilde{\Sigma}_s)_{ii} &= 0 \qquad\qquad\quad \text{if} \quad (\Lambda_{\mathbf{B}_s})_{ii} \leq 0. \end{aligned} \tag{32}$$

A time-dependent penalty matrix that automatically adjusts for stability according to (32) is given by

$$\tilde{\Sigma}_s = -(\Lambda_{\mathbf{B}_s} + |\Lambda_{\mathbf{B}_s}|)/2. \tag{33}$$

The final numerical energy estimate becomes

$$\begin{aligned} ||\mathbf{V}_L||^2_{\mathbf{J}(E_L\otimes P_\xi \otimes P_\eta \otimes I)} &= ||\mathbf{f}||^2_{\mathbf{J}(E_0\otimes P_\xi \otimes P_\eta \otimes I)} + ||(\mathbf{V}_\infty)_\mathbf{s}||^2_{\mathbf{B}_\mathbf{s}^+(P_\tau \otimes P_\xi \otimes E_0 \otimes I)} \\ &\quad + \mathbf{V_s}^T (P_\tau \otimes P_\xi \otimes E_0 \otimes I)\mathbf{B}_s^- \mathbf{V}_s \\ &\quad - ||\mathbf{V} - \mathbf{f}||^2_{\mathbf{J}(E_0\otimes P_\xi \otimes P_\eta \otimes I)} - ||\mathbf{V}_s - (\mathbf{V}_\infty)_\mathbf{s}||^2_{\mathbf{B}_s^+(P_\tau \otimes P_\xi \otimes E_0 \otimes I)}. \end{aligned} \tag{34}$$

In (34) the definition $||Z||^2_H = Z^T H Z$ is used for the norms, where Z is a vector and H is a positive definite matrix. As an example $||\mathbf{V}_L||^2_{\mathbf{J}(E_L\otimes P_\xi \otimes P_\eta \otimes I)} = \mathbf{V}_L^T \mathbf{J}(E_L \otimes P_\xi \otimes P_\eta \otimes I)\mathbf{V}_L$ in which $\mathbf{J}(E_L \otimes P_\xi \otimes P_\eta \otimes I)$ is positive definite. Moreover, $\mathbf{V}_L$ denotes the numerical solution restricted to the last time level.

We have proved

Proposition 3. *The discrete problem (22) is strongly stable and satisfies (34) if $\Sigma_i = -J$, $\Sigma_s = X_s \tilde{\Sigma}_s$ and $\tilde{\Sigma}_s = -(\Lambda_s + |\Lambda_s|)/2$ holds.*

Remark 3. Eq. (34) shows that the numerical energy estimate is similar to that of the continuous one shown in (15) with extra damping terms coming from the weak impositions of initial and boundary conditions.

Remark 4. The problem (22) is strongly stable since the estimate (34) contains the boundary data, see [23] for more details on stability definitions.

3.2. Conservation and weak form of the governing equations

In a conservation law, the total quantity of a conserved variable in any region changes only as a result of the flux through the boundaries of the region. To show that the solution is conserved, we integrate (8) in space and time and obtain

$$\iint_\Omega (JV)\big|_0^T \, d\xi \, d\eta + \int_0^T (F, G) \cdot n \, d\tau = 0, \tag{35}$$

in which $F = AV$ and $G = BV$. In this paper, we will however, rely on a broader definition of conservation motivated by the original proof of the Lax–Wendroff theorem [33]. We demand that all moments of the flux against an arbitrary test function telescope across the domain. This additional constraint demands an equivalence between the weak forms of the continuous and discrete operators [11].

We multiply (8) with an arbitrary test function $\phi(\tau, \xi, \eta) \in H^0$ that vanishes on the temporal and spatial boundaries followed by integration with respect to time and space as

$$\int_0^T \iint_\Omega \phi^T [(JV)_\tau + (AV)_\xi + (BV)_\eta] d\xi \, d\eta \, d\tau = 0. \tag{36}$$

Integration by parts and the fact that J, A and B are symmetric lead to

$$\int_0^T \iint_\Omega V^T [J\phi_\tau + A\phi_\xi + B\phi_\eta] d\xi \, d\eta \, d\tau = 0. \tag{37}$$

By adding and subtracting the term $V^T(J_\tau \phi + A_\xi \phi + B_\eta \phi)$ to the integral argument in (37) we obtain

$$\int_0^T \iint_\Omega V^T[(J\phi)_\tau + (A\phi)_\xi + (B\phi)_\eta]\,d\xi\,d\eta\,d\tau = \underbrace{\int_0^T \iint_\Omega V^T[(J_\tau + A_\xi + B_\eta)\phi]\,d\xi\,d\eta\,d\tau}_{:=RHS}. \tag{38}$$

In (38), the GCL leads to $RHS = 0$. Finally we split the integral argument on the left hand side and obtain

$$\tfrac{1}{2}\int_0^T \iint_\Omega V^T[(J\phi)_\tau + J\phi_\tau + J_\tau\phi + (A\phi)_\xi + A\phi_\xi + A_\xi\phi + (B\phi)_\eta + B\phi_\eta + B_\eta\phi]\,d\xi\,d\eta\,d\tau = 0. \tag{39}$$

Eqs. (37) and (39) are different weak forms of (8) including the broader definition of conservation mentioned above. The form (39) is of specific interest, since we use a scheme based on that form of splitting.

The discrete conservation is shown by multiplying the scheme in (22) from the left with $\phi^T(P_\tau \otimes P_\xi \otimes P_\eta \otimes I)$. The Kronecker rules (20), together with the SBP properties (18) lead to

$$\begin{aligned}
&\tfrac{1}{2}[\phi^T(-Q_\tau^T \otimes P_\xi \otimes P_\eta \otimes I)\mathbf{J}\mathbf{V} + \phi^T\mathbf{J}(-Q_\tau^T \otimes P_\xi \otimes P_\eta \otimes I)\mathbf{V} + \phi^T\tilde{P}\mathbf{J}_\tau\mathbf{V}]\\
+&\tfrac{1}{2}[\phi^T(P_\tau \otimes -Q_\xi^T \otimes P_\eta \otimes I)\mathbf{A}\mathbf{V} + \phi^T\mathbf{A}(P_\tau \otimes -Q_\xi^T \otimes P_\eta \otimes I)\mathbf{V} + \phi^T\tilde{P}\mathbf{A}_\xi\mathbf{V}]\\
+&\tfrac{1}{2}[\phi^T(P_\tau \otimes P_\xi \otimes -Q_\eta^T \otimes I)\mathbf{B}\mathbf{V} + \phi^T\mathbf{B}(P_\tau \otimes P_\xi \otimes -Q_\eta^T \otimes I)\mathbf{V} + \phi^T\tilde{P}\mathbf{B}_\tau\mathbf{V}] = 0,
\end{aligned} \tag{40}$$

in which all the penalty terms are ignored. Eq. (40) now becomes

$$\begin{aligned}
&\tfrac{1}{2}[(D_\tau\phi)^T\mathbf{J}\tilde{P}\mathbf{V} + (D_\tau\mathbf{J}\phi)^T\tilde{P}\mathbf{V} + \phi^T\mathbf{J}_\tau\tilde{P}\mathbf{V}]\\
+&\tfrac{1}{2}[(D_\xi\phi)^T\mathbf{A}\tilde{P}\mathbf{V} + (D_\xi\mathbf{A}\phi)^T\tilde{P}\mathbf{V} + \phi^T\mathbf{A}_\xi\tilde{P}\mathbf{V}]\\
+&\tfrac{1}{2}[(D_\eta\phi)^T\mathbf{B}\tilde{P}\mathbf{V} + (D_\eta\mathbf{B}\phi)^T\tilde{P}\mathbf{V} + \phi^T\mathbf{B}_\eta\tilde{P}\mathbf{V}] = 0.
\end{aligned} \tag{41}$$

By considering (20), and the fact that $\tilde{P}$ commutes with $\mathbf{J}$, $\mathbf{A}$, $\mathbf{B}$, $\mathbf{J}_\tau$, $\mathbf{A}_\xi$, $\mathbf{B}_\eta$ we obtain

$$\tfrac{1}{2}\mathbf{V}^T\tilde{P}[D_\tau\mathbf{J}\phi + (\mathbf{J}D_\tau\phi + \mathbf{J}_\tau\phi) + D_\xi\mathbf{A}\phi + (\mathbf{A}D_\xi\phi + \mathbf{A}_\xi\phi) + D_\eta\mathbf{B}\phi + (\mathbf{B}D_\eta\phi + \mathbf{B}_\eta\phi)] = 0. \tag{42}$$

The relation (42) mimics the weak conservative formulation (39) perfectly.

We have proved

Proposition 4. *The discrete problem (22) is conservative.*

4. Numerical experiments

We consider the two-dimensional constant coefficient symmetrized Euler equations in a deforming domain described by (1), where

$$V = [\frac{\bar{c}}{\sqrt{\gamma}\bar{\rho}}\rho, u, v, \frac{1}{\bar{c}\sqrt{\gamma(\gamma-1)}}T]^T. \tag{43}$$

In (43), ρ, u, v, T and γ are respectively the density, the velocity components in x and y directions, the temperature and the ratio of specific heats. An equation of state in form of $\gamma p = \bar{\rho}T + \rho\bar{T}$ closes the system (1), in which the bar sign denotes the state around which we have linearized. Moreover the matrices in (1) are

$$\hat{A} = \begin{pmatrix} \bar{u} & \bar{c}/\sqrt{\gamma} & 0 & 0 \\ \bar{c}/\sqrt{\gamma} & \bar{u} & 0 & \sqrt{\frac{\gamma-1}{\gamma}}\bar{c} \\ 0 & 0 & \bar{u} & 0 \\ 0 & \sqrt{\frac{\gamma-1}{\gamma}}\bar{c} & 0 & \bar{u} \end{pmatrix}, \quad \hat{B} = \begin{pmatrix} \bar{v} & 0 & \bar{c}/\sqrt{\gamma} & 0 \\ 0 & \bar{v} & 0 & 0 \\ \bar{c}/\sqrt{\gamma} & 0 & \bar{v} & \sqrt{\frac{\gamma-1}{\gamma}}\bar{c} \\ 0 & 0 & \sqrt{\frac{\gamma-1}{\gamma}}\bar{c} & \bar{v} \end{pmatrix}, \tag{44}$$

where $\gamma = 1.4$, $\bar{c} = 2$ and $\rho = 1$. These parameter values are used throughout the section while $\bar{u}$ and $\bar{v}$ are changed.

The deforming domain is chosen to be a portion of a ring-shaped geometry where the boundaries are moving while always coinciding with a coordinate line in the corresponding polar coordinate system, see Fig. 2. We transform the deforming domain from Cartesian coordinates, x, y, into polar coordinates, r, ϕ, and scale the polar coordinates such that the fixed domain in ξ, η coordinates becomes a square, see Fig. 2, as

$$\begin{aligned}
r(x,y,t) &= \sqrt{x(t)^2 + y(t)^2}, \quad \phi(x,y,t) = tan^{-1}(\tfrac{y(t)}{x(t)})\\
\xi(x,y,t) &= \tfrac{r(x,y,t)-r_0(t)}{r_1(t)-r_0(t)}, \qquad \eta(x,y,t) = \tfrac{\phi(x,y,t)-\phi_0(t)}{\phi_1(t)-\phi_0(t)}.
\end{aligned} \tag{45}$$

Note that the scaling depends on the movements of the boundaries of the deforming domain, and is defined by arbitrary functions of time through $r_0(t)$, $r_1(t)$, $\phi_0(t)$ and $\phi_1(t)$.

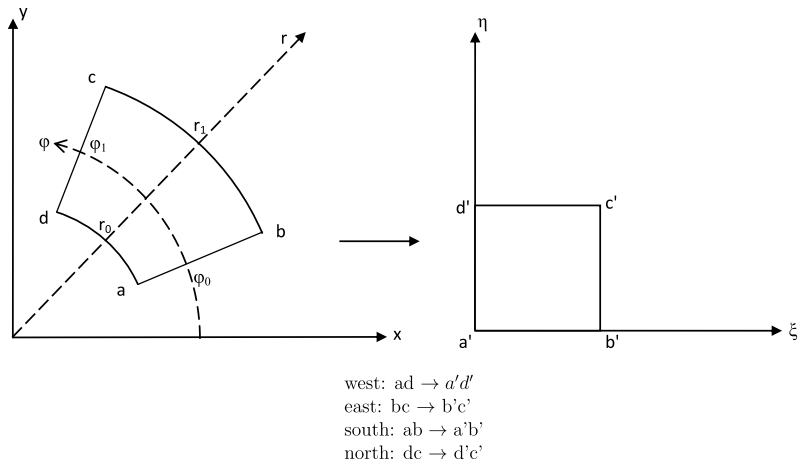

Fig. 2. A schematic of the Cartesian–polar transformation in the physical domain, the computational domain, and definition of r_0, r_1, ϕ_0 and ϕ_1.

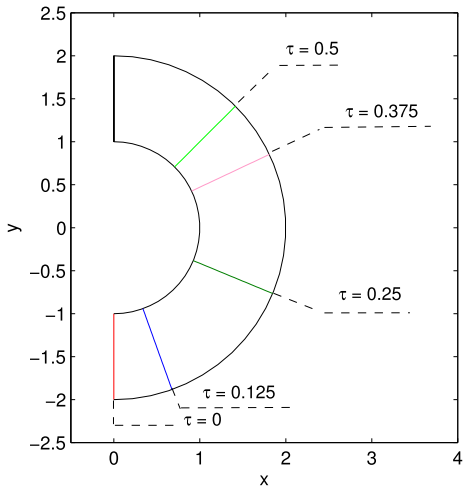

Fig. 3. A schematic of the deforming domain at five time levels.

4.1. Time-dependent automatic SAT formulations

To show that the scheme automatically imposes the correct number of boundary conditions, we move the boundaries by

$$\begin{aligned} r_0(t) &= 1, \quad \phi_0(t) = -\tfrac{\pi}{8} + \tfrac{3\pi}{8}\sin(2\pi t - \tfrac{\pi}{2}) \\ r_1(t) &= 2, \quad \phi_1(t) = \tfrac{\pi}{2}, \end{aligned} \tag{46}$$

and construct the matrices $\hat{A}$ and $\hat{B}$ by choosing $(\bar{u}, \bar{v}) = (1, 0)$.

The eigenvalue matrix Λ_C in (13), is evaluated at the moving boundary as

$$\Lambda_C = \begin{pmatrix} \omega & & & \\ & \omega & & \\ & & \omega - \mathcal{R}_2\bar{c} & \\ & & & \omega + \mathcal{R}_2\bar{c} \end{pmatrix}, \tag{47}$$

in which $\omega = J\eta_t + J\eta_x\bar{u} + J\eta_y\bar{v}$, $\mathcal{R}_2 = \sqrt{(J\eta_x)^2 + (J\eta_y)^2}$. As in (33), we construct $\tilde{\Sigma}_s$ such that the elements on the main diagonal are non-zero if and only if the corresponding eigenvalues are negative. Depending on the signs of the eigenvalues we can have zero (super-sonic outflow), one (sub-sonic outflow), three (sub-sonic inflow) or four boundary conditions (super-sonic inflow). Note that in time-dependent domains, the relative normal velocity between boundary and fluid distinguishes between inflow, outflow, sub- and super-sonic states.

A schematic of the deforming domain at five time levels is shown in Fig. 3. In Fig. 4, the number of boundary conditions imposed automatically at the moving boundary is depicted. Initially we have sub-sonic inflow and three boundary conditions

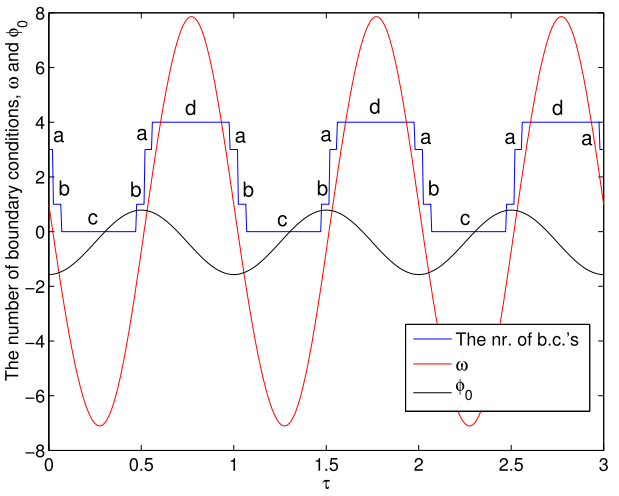

Fig. 4. The number of boundary conditions, the position of the moving boundary in terms of ϕ_0, and ω over time.

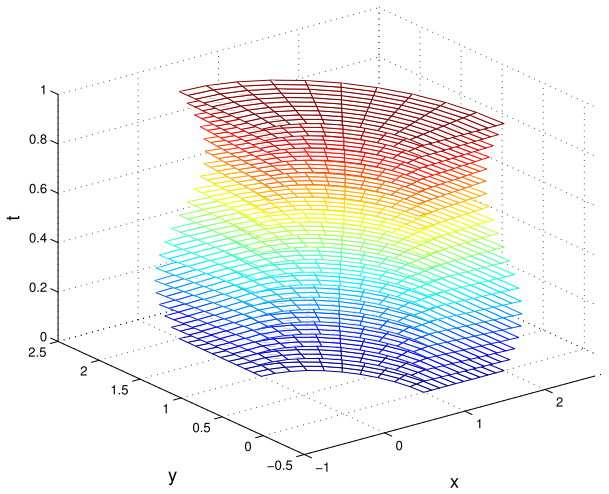

Fig. 5. A schematic of the deforming mesh at different times, order of accuracy.

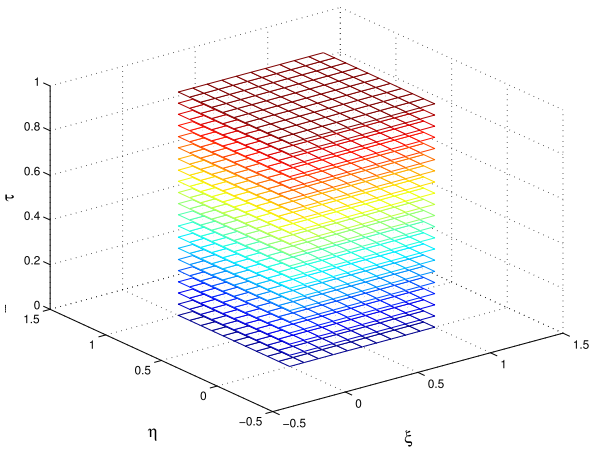

Fig. 6. A schematic of the fixed mesh at different times, order of accuracy.

are imposed (state a). Then the boundary encounters sub-sonic outflow which requires one boundary condition (state b). Next, no boundary conditions are imposed for the super-sonic outflow (state c). A sub-sonic outflow following by a sub-sonic inflow occurs afterwards which demands one and three boundary conditions respectively. Finally, in the case of super-sonic inflow (state d), four boundary conditions are imposed, and this procedure is continued automatically by the scheme.

4.2. Order of accuracy

We consider a deforming domain where the boundaries are moving by

$$r_0(t) = 1 - \tfrac{0.1}{2\pi}\sin(2\pi t), \quad \phi_0(t) = -\tfrac{0.5}{2\pi}\sin(2\pi t)$$
$$r_1(t) = 2 + \tfrac{0.2}{2\pi}\sin(2\pi t), \quad \phi_1(t) = \tfrac{\pi}{2} + \tfrac{0.5}{2\pi}\sin(2\pi t). \tag{48}$$

A schematic of the deforming and fixed domains at different time steps is presented in Fig. 5 and Fig. 6 respectively (note that these schematics are for illustration purposes only, the numerical experiments are carried out on finer meshes).

Here we use $(\bar{u}, \bar{v}) = (1, 1)$ and $\bar{c} = 2$ to construct the matrices $\hat{A}$ and $\hat{B}$. To verify the order of accuracy of our method, we use the manufactured solution V_∞

$$V_\infty = [sin(x-t), cos(x-t), sin(y-t), cos(y-t)]^T, \tag{49}$$

which is injected in (1) through a forcing function. The characteristic boundary conditions (13) are automatically imposed by the scheme.

Table 1
Convergence rates at $T = 1$, for a sequence of mesh refinements, SBP21 in space, SBP84 in time ($L = 41$).

N, M	21	41	81	161	201
ρ	1.952	1.988	1.995	1.998	2.001
u	2.049	2.001	2.002	1.999	2.001
v	1.955	1.987	1.996	1.998	1.999
p	2.001	1.996	1.996	1.998	1.999

Table 2
Convergence rates at $T = 1$, for a sequence of mesh refinements, SBP42 in space, SBP84 in time ($L = 81$).

N, M	21	41	81	161	201
ρ	3.248	3.177	3.099	3.052	3.032
u	3.388	3.238	3.166	3.107	3.077
v	3.198	3.141	3.057	3.026	3.017
p	2.912	2.800	2.989	3.034	3.037

Table 3
Convergence rates at $T = 1$, for a sequence of mesh refinements, SBP63 in space, SBP84 in time ($L = 201$).

N, M	21	31	41	51	61	71
ρ	5.780	4.681	4.502	4.379	4.320	4.296
u	6.120	4.531	4.585	4.588	4.575	4.558
v	6.138	4.300	4.179	4.215	4.249	4.268
p	5.701	4.124	4.267	4.340	4.380	4.402

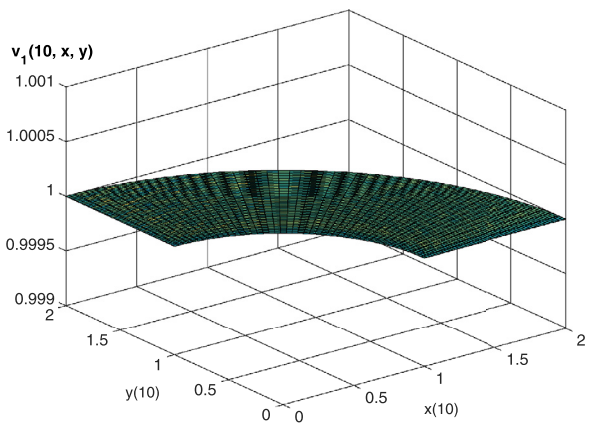

Fig. 7. The ρ component of the solution at $T = 40$.

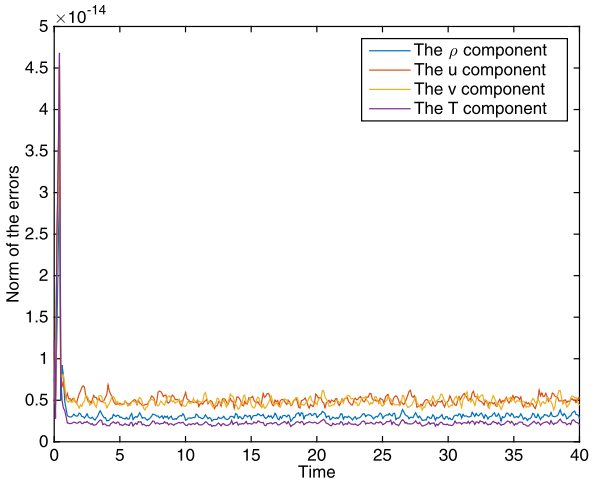

Fig. 8. The norm of the error for all solution components versus time.

The convergence rate is defined as

$$p = \frac{log\frac{||V_{\infty}^{(1)} - V^{(1)}||_{\tilde{P}}}{||V_{\infty}^{(2)} - V^{(2)}||_{\tilde{P}}}}{log\frac{(NM)^{(1)}}{(NM)^{(2)}}}, \tag{50}$$

where superscripts (1) and (2) denote two mesh levels with $(N \times M)^{(1)}$ and $(N \times M)^{(2)}$ grid points respectively, also $\tilde{P} = E_L P_\tau \otimes P_\xi \otimes P_\eta \otimes I$. In order to show the convergence rate in space we use the 5th order accurate SBP84 in time.

The numerical solution in our experiments converges to the exact solution at $T = 1$ with the convergence rates presented in Tables 1, 2 and 3. The convergence rates are in agreement with the theory mentioned above, and we conclude that our scheme works as it should.

4.3. Free-stream preservation

Consider the domain described in (48) with $(\bar{u}, \bar{v}) = (1, 1)$ when constructing the matrices $\hat{A}$ and $\hat{B}$. In order to show that the scheme in (22) preserves the state of a uniform flow, we use the manufactured solution

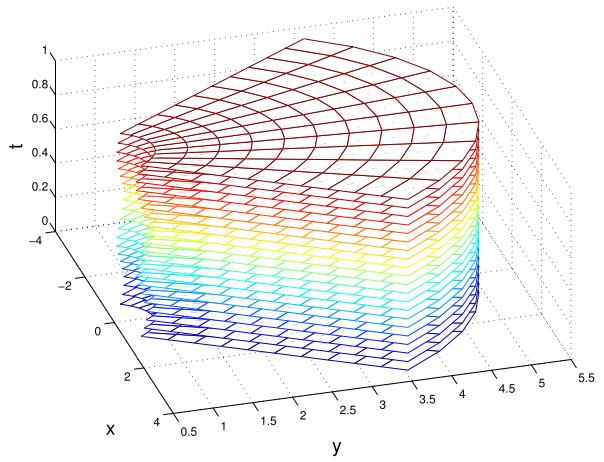

Fig. 9. A schematic of the deforming mesh at different times, sound propagation.

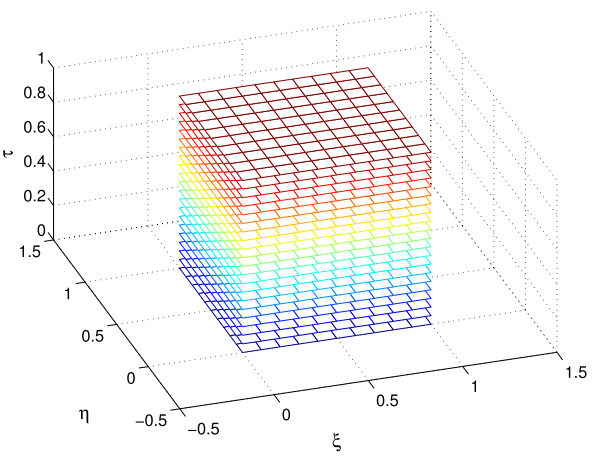

Fig. 10. A schematic of the fixed mesh at different times, sound propagation.

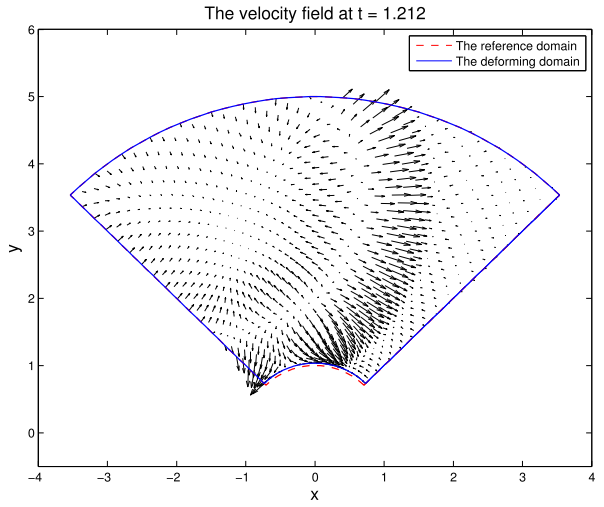

Fig. 11. The global velocity field.

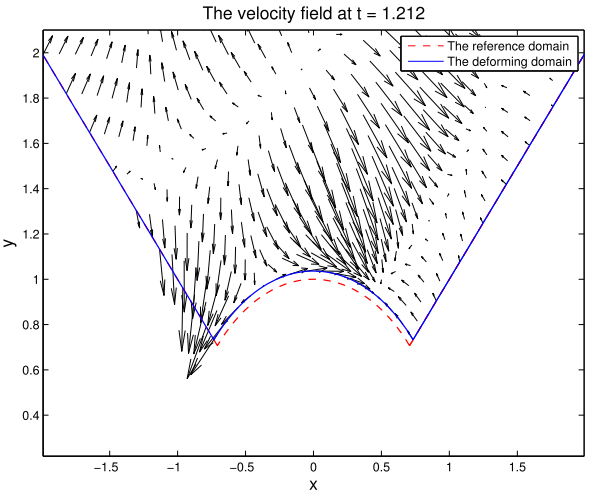

Fig. 12. A blow-up of the velocity field.

$$V_\infty = [1, 1, 1, 1]^T . \tag{51}$$

The characteristic boundary conditions (13) are automatically imposed by the scheme. We use the 5th order accurate SBP84 in time ($L = 100$) and 3rd order accurate SBP42 in space ($N = M = 50$).

The uniform flow (examplified by the density component) is preserved up to $T = 40$ as presented in Fig. 7. Moreover, the norm of the error (the difference between the numerical and manufactured solution) versus time is on machine precision level, see Fig. 8.

4.4. The sound propagation application

We consider sound propagation in a deforming domain where the west boundary is moving and other boundaries are fixed. A schematic of the deforming and fixed domains at different time steps is presented in Figs. 9 and 10 (note that these schematics are for illustration purposes only, the numerical experiments are carried out on finer meshes). The movements are defined by

$$\begin{aligned} r_0(t) &= 1 + \sin(4\pi t)/(4\pi), \quad & \phi_0(t) &= \pi/4, \\ r_1(t) &= 5, & \phi_1(t) &= 3\pi/4. \end{aligned} \tag{52}$$

We manufacture $\bar{u}$ and $\bar{v}$ such that the mean flow satisfies the solid wall no-penetration condition at the moving boundary by

$$(\bar{u}, \bar{v}) = (x_\tau, y_\tau)/\exp(\xi). \tag{53}$$

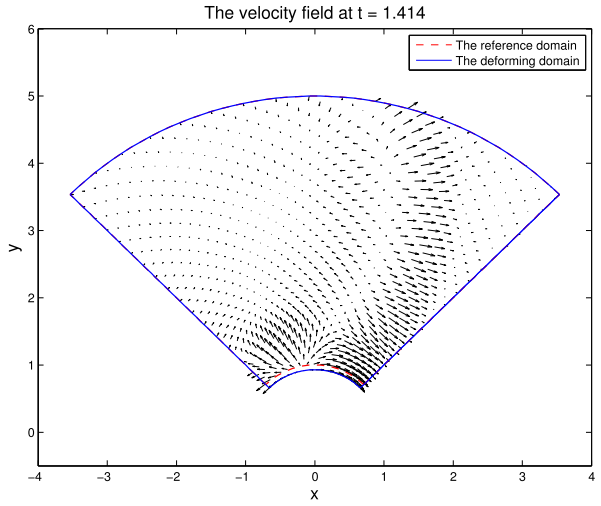

Fig. 13. The global velocity field.

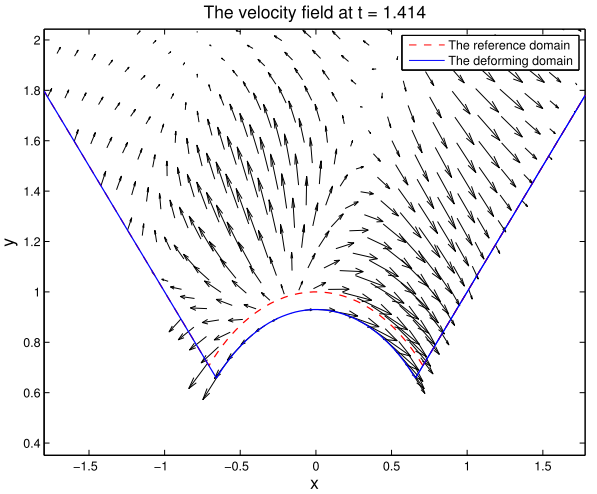

Fig. 14. A blow-up of the velocity field.

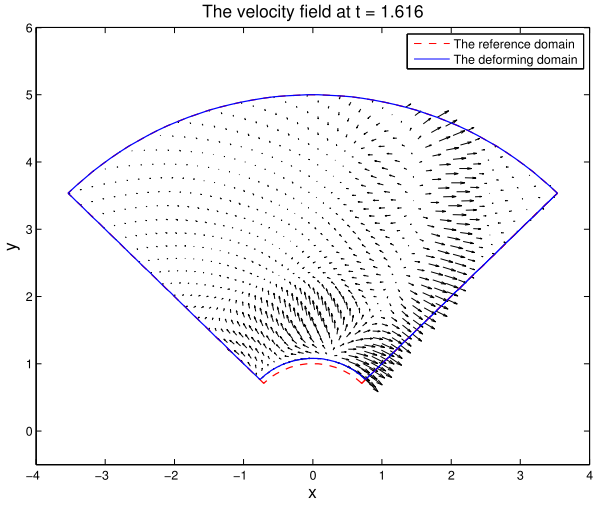

Fig. 15. The global velocity field.

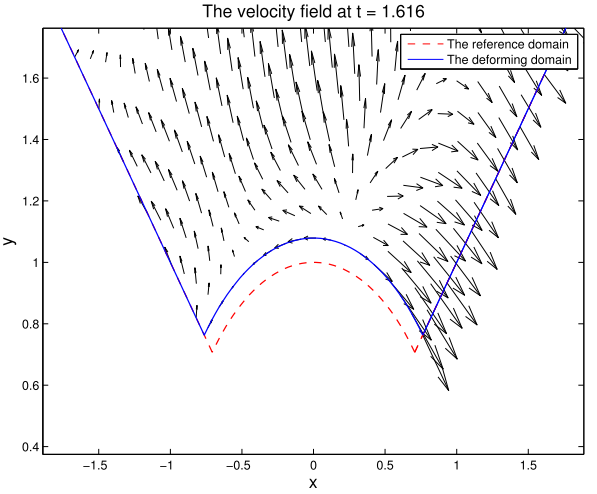

Fig. 16. A blow-up of the velocity field.

Consider the eigenvalue matrix, $C = X\Lambda X^T$ evaluated at the west boundary, in which $\Lambda = \mathcal{R}_1 \text{diag}(\hat{\omega}, \hat{\omega}, \hat{\omega} - \bar{c}, \hat{\omega} + \bar{c})$, where $\hat{\omega} = (J\xi_t + J\xi_x \bar{u}_b + J\xi_y \bar{v}_b)/\mathcal{R}_1$ and $\mathcal{R}_1 = \sqrt{(J\xi_x)^2 + (J\xi_y)^2}$. The no-penetration condition for the mean flow results in $\hat{\omega} = 0$, which takes (14) to

$$||V(T,\xi,\eta)||_J^2 = ||f(\xi,\eta)||^2 - \mathcal{R}_1 \int_0^T \int_0^1 \bar{c}(\tilde{v}_4^2 - \tilde{v}_3^2) d\eta + \text{BT}. \tag{54}$$

In (54), $\tilde{V} = X^T V = [\tilde{v}_1, \tilde{v}_2, \tilde{v}_3, \tilde{v}_4]^T$, and BT is the contribution at the other boundaries. Any boundary condition in form of $\tilde{v}_3 = \pm \tilde{v}_4$ is well-posed. We choose $\tilde{v}_3 + \tilde{v}_4 = 0$, which is the no-penetration boundary condition. Also we impose characteristic boundary conditions with zero data at the other boundaries, and initialize the solution with zero data for density and velocities, together with an initial pressure pulse centered at $(-1.5, 3.5)$.

The velocity field with tangential flow close to the solid wall, the pressure distribution and the rate of dilatation at five different time levels are presented in Figs. 11–30. We have used SBP42 in both space and time ($N = M = 50$ and $L = 100$) to obtain these results.

The reference domain in Figs. 11–30 illustrate the movements of the south boundary relative to its initial location. As seen in Figs. 11–20 the flow stays tangential to the moving solid boundary all the time, as it should for an Euler solution. The pressure pulse and the corresponding rate of dilatation move from left to right, and leave the domain as time passes.

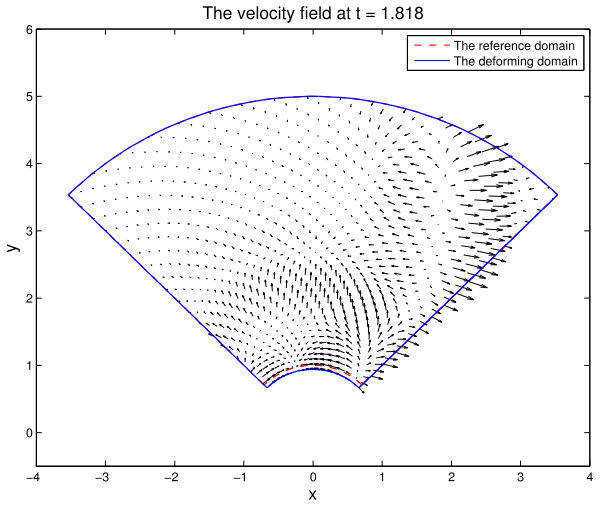

Fig. 17. The global velocity field.

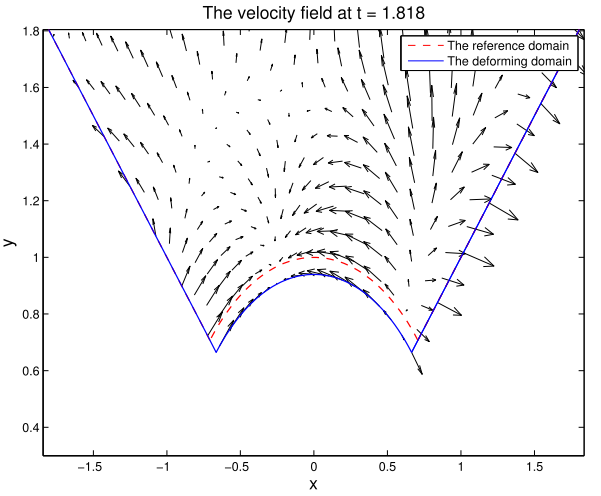

Fig. 18. A blow-up of the velocity field.

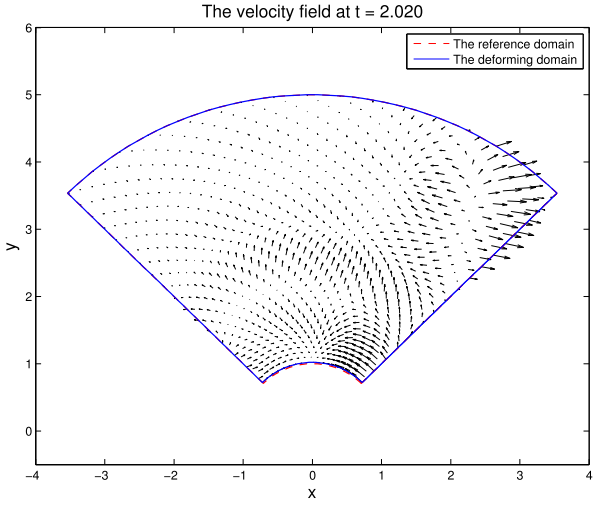

Fig. 19. The global velocity field.

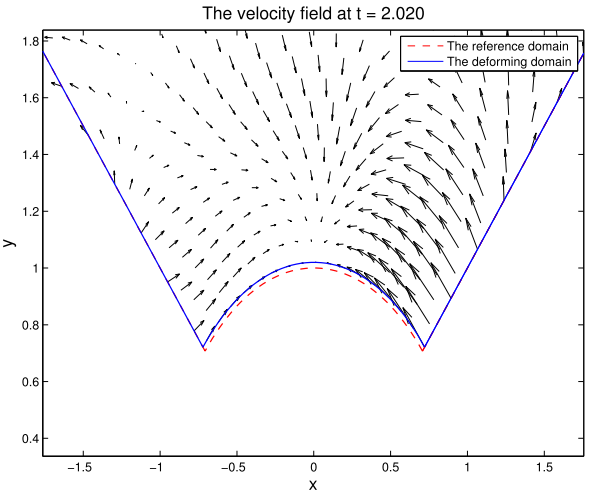

Fig. 20. A blow-up of the velocity field.

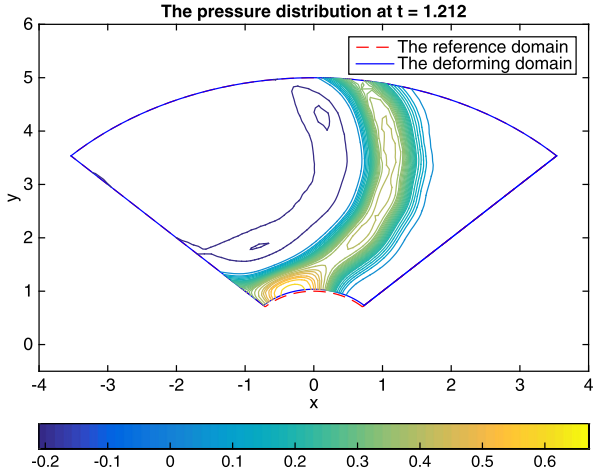

Fig. 21. The pressure distribution.

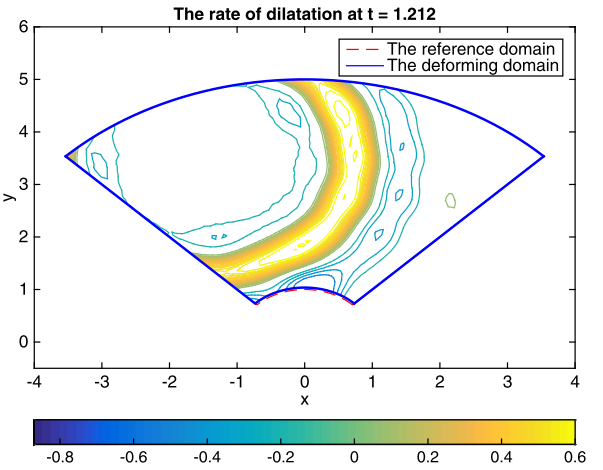

Fig. 22. The rate of dilatation.

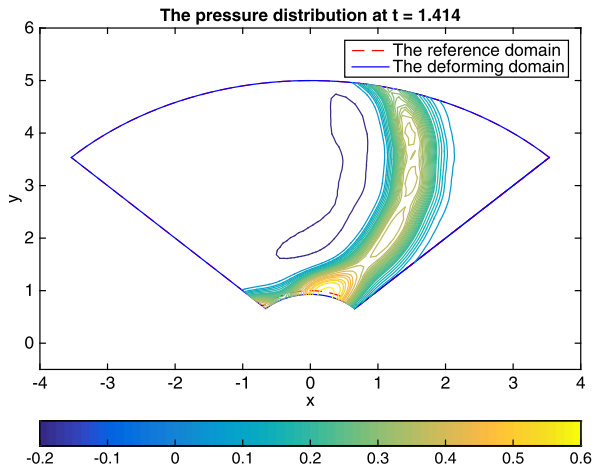

Fig. 23. The pressure distribution.

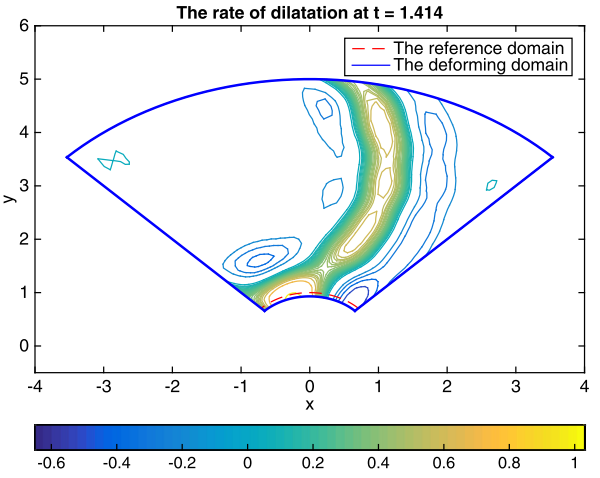

Fig. 24. The rate of dilatation.

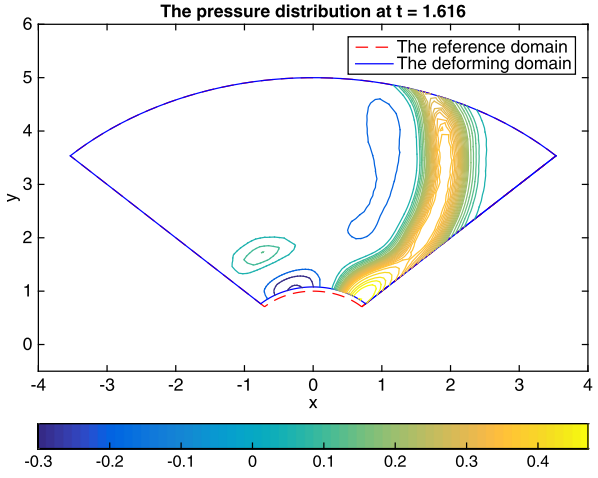

Fig. 25. The pressure distribution.

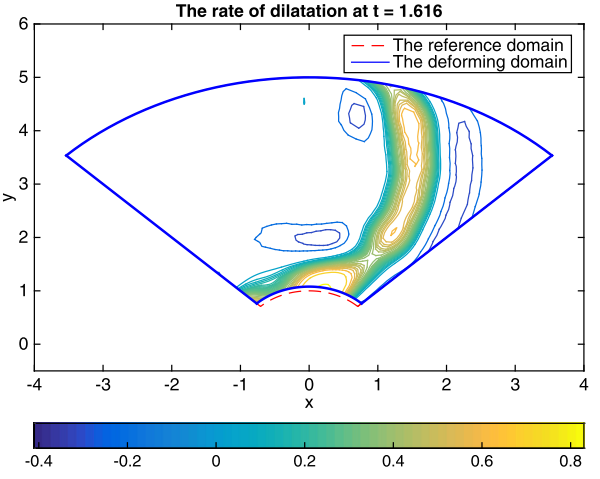

Fig. 26. The rate of dilatation.

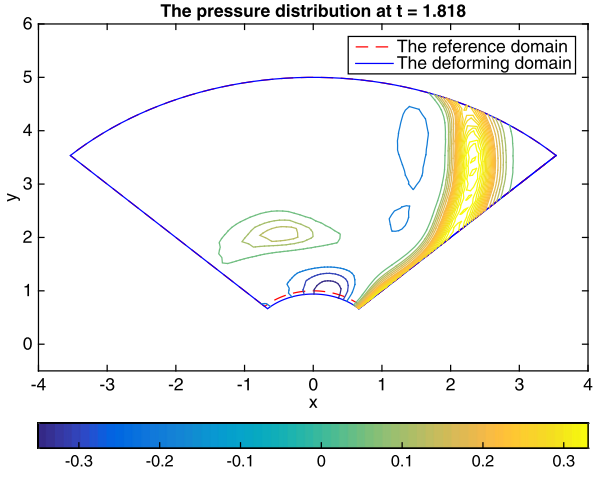

Fig. 27. The pressure distribution.

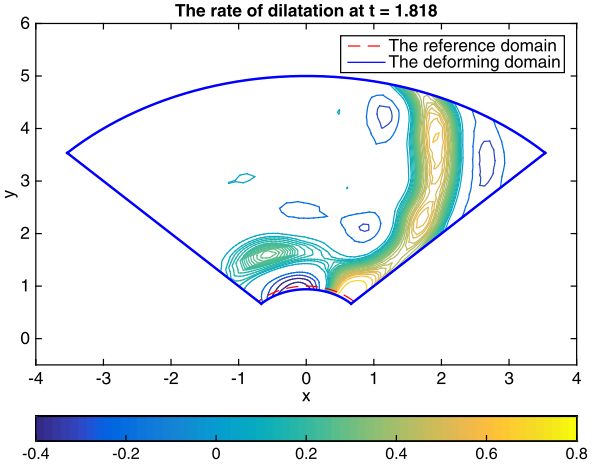

Fig. 28. The rate of dilatation.

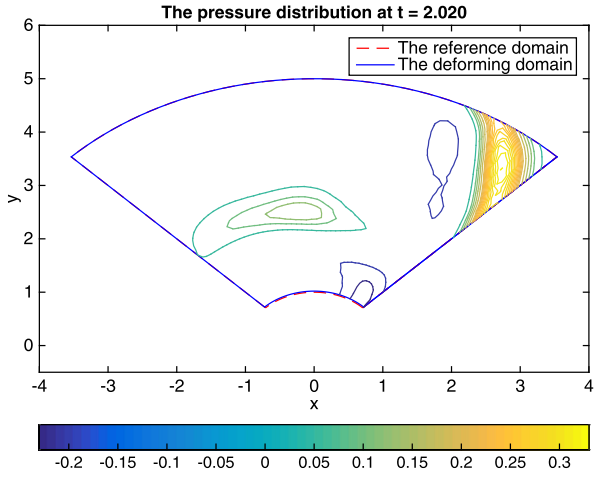

Fig. 29. The pressure distribution.

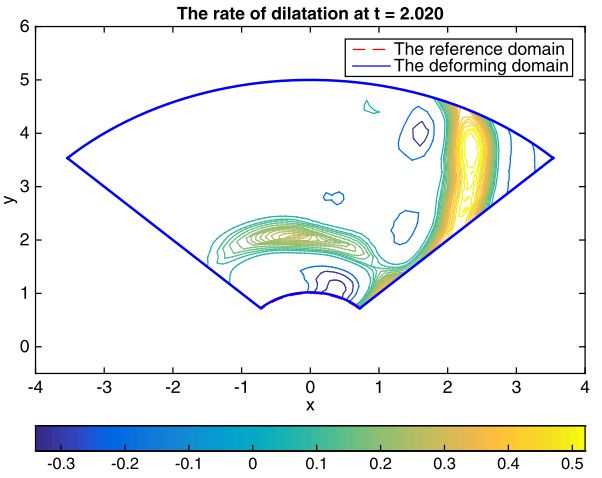

Fig. 30. The rate of dilatation.

5. Summary and conclusions

We have considered a constant coefficient hyperbolic system of equations in time-dependent curvilinear coordinates. The system is transformed into a fixed coordinate frame, resulting in variable coefficient systems. We show that the energy method applied to the transformed systems together with time-dependent appropriate boundary conditions leads to strongly well-posed problem. The continuous energy estimate that we obtain provides the target for the numerical approximations.

By using a special splitting technique, summation-by-parts operators in space and time, weak imposition of the boundary and initial conditions and the discrete energy method, a fully-discrete strongly stable high order accurate and conservative numerical scheme is constructed. The fully-discrete energy estimate is similar to the continuous one with small added damping terms. Furthermore, by the use of SBP operators in time, the Geometric Conservation Law is proven to hold numerically.

We have tested the scheme for high order accurate SBP operators in space and time using the method of manufactured solution. It was shown that the scheme automatically imposes the correct number of boundary conditions for the time-dependent domain. Numerical calculations corroborate the stability and accuracy of the fully-discrete approximations, and free-stream preservation was shown. Finally, as an application, sound propagation by the linearized Euler equations in a deforming domain was illustrated.

References

[1] J. Nordström, J. Gong, E.V.D. Weide, M. Svärd, A stable and conservative high order multi-block method for the compressible Navier–Stokes equations, J. Comput. Phys. 228 (2009) 9020–9035.
[2] J. Nordström, M.H. Carpenter, Boundary and interface conditions for high order finite difference methods applied to the Euler and Navier–Stokes equations, J. Comput. Phys. 148 (1999) 621–645.
[3] J. Nordström, M.H. Carpenter, High-order finite difference methods, multidimensional linear problems and curvilinear coordinates, J. Comput. Phys. 173 (2001) 149–174.
[4] J. Nordström, R. Gustaffsson, High order finite difference approximations of electromagnetic wave propagation close to material discontinuities, J. Sci. Comput. 18 (2003) 215–234.
[5] M. Svärd, M.H. Carpenter, J. Nordström, A stable high-order finite difference scheme for the compressible Navier–Stokes equations: far-field boundary conditions, J. Comput. Phys. 225 (2007) 1020–1038.
[6] J.E. Kozdon, E.M. Dunham, J. Nordström, Simulation of dynamic earthquake ruptures in complex geometries using high-order finite difference methods, J. Sci. Comput. 55 (2013) 92–124.
[7] X. Deng, M. Mao, G. Tu, H. Zhang, Y. Zhang, High-order and high accurate CFD methods and their applications for complex grid problems, Commun. Comput. Phys. 11 (2012) 1081–1102.
[8] M. Svärd, J. Nordström, Review of summation-by-parts schemes for initial–boundary-value problems, J. Comput. Phys. 268 (2014) 17–38.
[9] D.C.D.R. Fernández, J.E. Hicken, D.W. Zingg, Review of summation-by-parts operators with simultaneous approximation terms for the numerical solution of partial differential equations, Comput. Fluids 95 (2014) 171–196.
[10] C. Farhat, P. Geuzaine, C. Grandmont, The discrete geometric conservation law and the nonlinear stability of ALE schemes for the solution of flow problems on moving grids, J. Comput. Phys. 174 (2001) 669–694.
[11] M.H. Carpenter, J. Nordström, D. Gottleib, A stable and conservative interface treatment of arbitrary spatial accuracy, J. Comput. Phys. 148 (1999) 341–365.
[12] P.D. Thomas, C.K. Lombard, Geometric conservation law and its application to flow computations on moving grids, AIAA J. 17 (1979) 1030–1037.
[13] J. Nordström, T. Lundquist, Summation-by-parts in time, J. Comput. Phys. 251 (2013) 487–499.
[14] T. Lundquist, J. Nordström, The SBP-SAT technique for initial value problems, J. Comput. Phys. 270 (2014) 86–104.
[15] J.E. Kozdon, E.M. Dunham, J. Nordström, Interaction of waves with frictional interfaces using summation-by-parts difference operators: weak enforcement of nonlinear boundary conditions, J. Sci. Comput. 50 (2012) 341–367.
[16] K. Yee, Numerical solution of initial boundary value problems involving Maxwell's equations in isotropic media, IEEE Trans. Antennas Propag. 14 (1966) 302–307.

[17] J.S. Hesthaven, T. Warburton, Nodal high-order methods on unstructured grids: I. Time-domain solution of Maxwell's equations, J. Comput. Phys. 181 (2002) 186–221.
[18] S. Abarbanel, D. Gottlieb, Optimal time splitting for two- and three-dimensional Navier–Stokes equations with mixed derivatives, J. Comput. Phys. 41 (1981) 1–33.
[19] E. Turkel, Symmetrization of the fluid dynamics matrices with applications, Math. Comput. 27 (1973) 729–736.
[20] C. Bailly, D. Juve, Numerical solution of acoustic propagation problems using linearized Euler equations, AIAA J. 38 (2000) 22–29.
[21] H. Guillard, C. Farhat, On the significance of the geometric conservation law for flow computations on moving meshes, Comput. Methods Appl. Mech. Eng. 190 (2000) 1467–1482.
[22] B. Sjögreen, H.C. Yee, M. Vinokur, On high order finite-difference metric discretizations satisfying GCL on moving and deforming grids, J. Comput. Phys. 265 (2014) 211–220.
[23] B. Gustafsson, H.O. Kreiss, J. Oliger, Time Dependent Problems and Difference Methods, John Wiley and Sons, 1995.
[24] B. Strand, Summation by parts for finite difference approximations of d/dx, J. Comput. Phys. 29 (1994) 47–67.
[25] M. Svärd, J. Nordström, On the order of accuracy for difference approximations of initial boundary value problems, J. Comput. Phys. 218 (2006) 333–352.
[26] S.S. Abarbanel, A.E. Chertock, Strict stability of high-order compact implicit finite-difference schemes: the role of boundary conditions for hyperbolic PDEs, I, J. Comput. Phys. 160 (2000) 42–66.
[27] S.S. Abarbanel, A.E. Chertock, A. Yefet, Strict stability of high-order compact implicit finite-difference schemes: the role of boundary conditions for hyperbolic PDEs, II, J. Comput. Phys. 160 (2000) 67–87.
[28] M.H. Carpenter, D. Gottlieb, Spectral methods on arbitrary grids, J. Comput. Phys. 129 (1996) 74–86.
[29] D.C.D.R. Fernández, P.D. Boom, D.W. Zingg, A generalized framework for nodal first derivative summation-by-parts operators, J. Comput. Phys. 266 (2014) 214–239.
[30] C.F.V. Loan, The ubiquitous Kronecker product, J. Comput. Appl. Math. 123 (2000) 85–100.
[31] J. Nordström, Conservative finite difference formulations, variable coefficients, energy estimates and artificial dissipation, J. Sci. Comput. 29 (2006) 375–404.
[32] R. Hixon, Numerically consistent strong conservation grid motion for finite difference schemes, AIAA J. 38 (2000) 1586–1593.
[33] P. Lax, B. Wendroff, Systems of conservation laws, Commun. Pure Appl. Math. 13 (1960) 217–237.